International Journal of Heat and Mass Transfer 169 (2021) 120921

Contents lists available at ScienceDirect

International Journal of Heat and Mass Transfer

journal homepage: www.elsevier.com/locate/hmt

Frequency response analysis for the determination of thermal conductivity and water transport in MOF adsorbent coatings for heat transformation

Eric Laurenz [a,b,*], Gerrit Füldner [a,*], Andreas Velte [a], Lena Schnabel [a], Gerhard Schmitz [b]

[a] Fraunhofer Institute for Solar Energy Systems ISE, Department of Heating and Cooling Technologies, Heidenhofstr. 2, 79110 Freiburg, Germany
[b] Hamburg University of Technology, Institute of Engineering Thermodynamics, Denickestr. 17, 21073 Hamburg, Germany

ARTICLE INFO

Article history:
Received 15 July 2020
Revised 5 November 2020
Accepted 5 December 2020

Keywords:
Adsorption kinetics
Adsorption dynamics
Heat transfer
Thermal conductivity
Aluminum fumarate
Metal organic framework
Adsorbent coating
Adsorption chillers
Temperature frequency response
Non-isothermal
Thermal frequency response

ABSTRACT

In this paper we focus on the differentiation and quantification of different heat and mass transfer phenomena governing the overall sorption dynamics, for the example of a binder-based aluminium fumarate (Alfum) coating for heat transformation applications with water as refrigerant. The methodological emphasis is on extending the volume swing frequency response (FR) method to problems with strong heat transfer limitation. The heat and mass transfer parameters are mapped to the sample temperature and loading state, in order to be able to reproduce the strongly non-linear behaviour exhibited under application conditions. Based on a model with discretised heat transfer and linear driving force (LDF)-simplified micropore diffusion, the thermal conductivity of the samples was identified as about 0.07 W/(m K), and the LDF time constant between 0.1 and 3 s^{-1} at 40°C with a U-shaped loading dependency and an Arrhenius-type temperature dependency. The method is validated by comparing a measured large temperature jump experiment to the results from a non-linear simulation informed solely by these parameters obtained from the new FR-based method.

1. Introduction

Adsorption chillers are an environmentally friendly solution for the valorisation of waste or solar heat for cooling demands [1,2]. The metal organic framework (MOF) aluminium fumarate is a promising candidate in applications with low differences among the driving temperature, rejection temperature and cooling temperature [3], like data centre cooling where water-cooled CPUs provide driving temperatures of up to 60°C or more [4].

Binder-based coatings are a promising approach to increase the volume-specific cooling power (VSCP) in order to reduce costs [5] while keeping a reasonably high coefficient of performance. Coatings allow for substantially better heat transfer compared to state-of-the-art loose-grain configurations [6].

For efficient design and optimisation of adsorber heat exchangers (Ad-HX), non-linear dynamic models of the sorption process are required in order to avoid costly and time-consuming trial-and-error prototyping [7]. Alongside with the adsorption equilibria, the adsorption enthalpy and the specific heat capacity, these models require detailed descriptions of the physical heat and mass transfer processes in the adsorbent coating.

Frequency response analysis (FRA) is a proven method for the determination of heat and mass transfer processes in adsorption systems since the 1960s [8–14]: From a set equilibrium state, an adsorbent sample is exposed to an, e.g., sinusoidal, periodical fluctuation of one variable (excitation) while the response of one or more other variables is recorded. The complex response, i.e. amplitude and phase shift, as a function of the frequency of the excitation signal contains the entire dynamic information of the sample. The method has several principal advantages compared to the step response methods usually used [7] in the field of heat transformation applications:

- Separation of different transport processes as they are visible at different frequencies depending on their time constant and with different patterns depending on the transport mechanisms
- High resolution of the thermodynamic state as, during the experiment, the system is kept in a small region around a constant equilibrium state

* Corresponding authors.
E-mail addresses: eric.laurenz@ise.fraunhofer.de (E. Laurenz), gerrit.fueldner@ise.fraunhofer.de (G. Füldner).

https://doi.org/10.1016/j.ijheatmasstransfer.2021.120921

Nomenclature

Abbreviations

0D	Zero-dimensional, lumped
Ad-HX	Adsorber heat exchanger
CAS	Computer algebra system
FR	Frequency response
FRA	Frequency response analysis
HT	Heat transfer
LDF	Linear driving force
LTJ	Large temperature jump
maD	Macropore diffusion
miD	Micropore diffusion
NETD	Noise equivalent temperature difference
RMSD	Root mean square deviation
PFG NMR	Pulsed-field gradient nuclear magnetic resonance

Variables

T	Temperature (K)
p	Pressure (Pa)
X	Loading ($kg_{adsorbed}/kg_{sorbent,dry}$)
X_{eff}	Effective loading ($kg_{adsorbed}/kg_{composite,dry}$)
D	Diffusivity (m^2/s)
h	(Effective) Heat transfer coefficient ($W/(m^2K)$)
d	Layer thickness, diameter (m)
$\boldsymbol{P}$	Vector of identified parameters (any unit)
E	Error functional, weighted root mean squared difference (-)
λ	Thermal conductivity (W/(m K))
V	Volume (m^3)
A	Surface area (m^2), adsorption potential (J/kg), Amplitude (any unit)
R	Universal gas constant (J/(mol K))
R_w	Specific gas constant of water (J/(kg K))
ρ	Density (kg/m^3)
m	Mass (kg)
τ	Time constant (s)
f	Frequency (Hz)
ϕ	Phase shift (rad)
ψ	Empty chamber pressure correction factor (-)
t	Time (s)
s	Laplace variable (1/s)
G_{pV}	Complex pressure volume transfer function (Pa/m^3)
G_{XV}	Complex loading volume transfer function ($((kg/kg)/m^3$)
c_p	Specific heat capacity (J/(kg K))
G_{TX}	Complex temperature loading transfer function (K/(kg/kg))
G_{TV}	Complex temperature volume transfer function (K/m^3)
j	Imaginary unit (-)
M	Molar mass (kg/mol)
k	Kinetic coefficient (1/s)
$\dot{q}$	Heat flux (W/m^2)
x	Space variable (m)
$\dot{n}$	Molar flux ($mol/(m^2\ s)$)
r	Radius (m)
K_T	Slope of the isobar ((kg/kg)/K)
K_p	Slope of the isotherm per pressure ((kg/kg)/Pa)
c	Concentration (mol/m^3)
ε_P	Macroporosity (m^3/m^3)
α	Model coefficient: $\alpha = K_p \rho_s R_w T_0/\varepsilon_P$ (-)
β	Model coefficient: $\beta = Ah + c_p m_s s$ (W/K)
K_c	Slope of the isotherm per concentration ($((kg/kg)/(mol/m^3)$)
γ	Model coefficient: $\gamma = \Delta h_s K_T m_s$ (J/K)
Δh_s	Differential adsorption enthalpy ($J/kg_{adsorbed}$)
N	Number of observations
$\boldsymbol{y}$	Vector of all measurands per frequency (any unit)
$\boldsymbol{W}$	Weighing matrix (any unit)
$\boldsymbol{k}$	Vector of individual measurands over all frequencies (any unit)
σ	LDF curvature factor (-)
E_a	Activation energy (J/mol)

Indices & superscripts

$\sim$	Laplace transformed of the deviation from the temporal mean value
$\hat{}$	Amplitude, deviation from the temporal mean, best estimate
$-$	Spatial mean value
sat	At saturation condition (liquid vapour equilibrium)
sp	(Ad)sorbed phase, adsorbate
w	Water
s	(Ad)sorbent, (ad)sorption
0	Temporal mean value
cal	At calibration conditions, blank measurement
ch	(Measurement) chamber
Btm	Bottom of the composite (at the interface to the sample support)
mi, miD	Micropore (diffusion, LDF-approximated)
maD	Macropore diffusion
LDF	Linear driving force
eq	At equilibrium
srf	Surface of the composite/sample
cmp	Composite
ct	Coating
f	Per Frequency
exp	Experimental
rel	Relative
ad	Adsorbate
g	Gas

- Easily scalable accuracy by changing the duration of the experiment, i.e. changing the number of periods measured per frequency
- Usage of locally linearised models with constant coefficients without accuracy loss as, in the small state region, non-linearities may typically be neglected
- Measurements in the frequency domain allow for usage of model solutions directly in the Laplace domain without the need for back-transformation to the time domain
- Computationally inexpensive parameter identification as, for linearised models in the Laplace domain, analytical solutions can be derived in most cases

These advantages outweigh the considerable experimental and data processing effort, especially if a quantitative differentiation between different transport processes and their dependency on the thermodynamic state (temperature, loading, pressure) of the system is required.

In the literature on FRA, the “heat effect”, i.e. the sample’s non-isothermal temperature evolution [11,15], is (if at all) handled as a small parasitic effect disturbing the understanding of the mass transfer processes. It was either mitigated by applying a flow-through system [12], where a continuous gas flow increases the heat transfer by convection, or taken into account and corrected using the thermal frequency response [16,17], where the

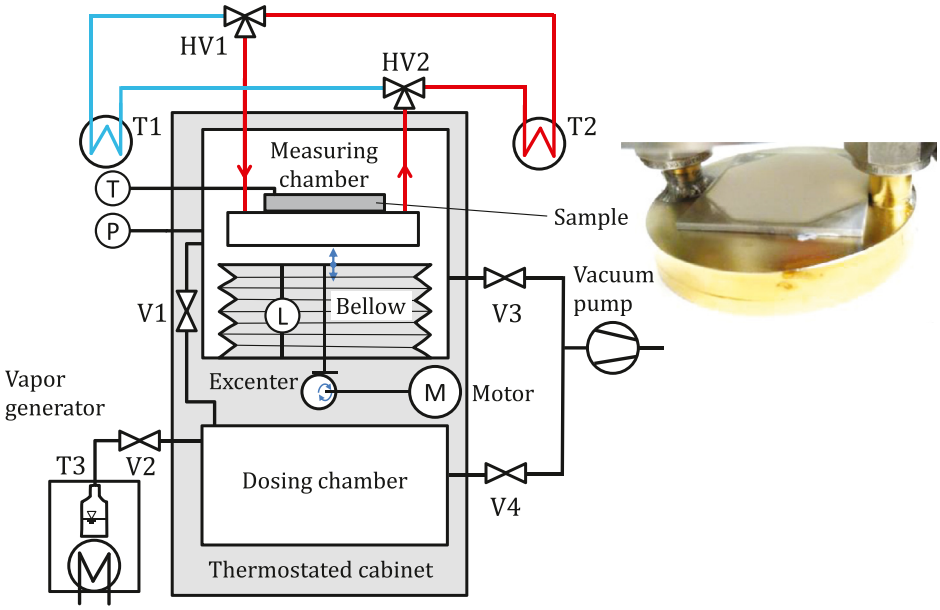

Fig. 1. Sorption kinetic setup for frequency response (FR), large temperature jump (LTJ) and large pressure jump (LPJ) experiments with absolute and differential equilibrium measurements (source: [18]).

response sample surface temperature is measured using a costly high-precision fast IR detector cooled with liquid helium. For heat transformation applications, the case is different, with the heat effect being the principal application motivation. This requires a sound understanding of the heat transfer processes as much as of the mass transfer processes, and the heat effect becomes an important source of information.

In this paper, we present a FRA-based determination of the heat and mass transfer processes, namely thermal conduction and micropore diffusion, in aluminium fumarate coatings that are relevant for heat transformation applications. This is part of a comprehensive approach that also allows obtaining adsorption equilibria and adsorption enthalpies [18] alongside with the sorption dynamics, in a single measurement procedure, under exactly the same measurement conditions and for a very narrow region in the thermodynamic state space. The loading and temperature dependency of the obtained transport properties is mapped. This allows us to simulate a large temperature jump (LTJ) under realistic application conditions and to validate the parametrised model by comparing the simulation to experimental results.

2. Experiments

2.1. Material

Aluminium sample plates (5 × 5 cm²) were partly coated ($A_{ct} = 18.9$ cm²) with aluminium fumarate (Basolite® A520, BASF, [19,20]) using a silicon binder, and characterised as described before [18]. The coating thickness d_{ct} was varied (0.14, 0.24, 0.61 mm), resulting in different coating dry masses (134, 217, 563 mg). The coating dry density was calculated as $\rho_{cmp} = m_{cmp}/(A_{ct}d_{ct})$ (0.51, 0.48, 0.49 g/cm³). The dry adsorbent content of the coating, by mass, was aimed at 0.75 and was confirmed, on average, for the three samples (0.72, 0.79, 0.80) by uptake comparison [18]. Sample details are given in the Supplementary Information (Table S1) and in a separate publication on the thermodynamic equilibrium properties of the samples [18]. The specific heat capacity of the coatings was measured for different water loadings (0–0.35 kg/kg$_{cmp}$) and temperatures (30–90°C) by differential scanning calorimetry (publication in preparation). Results were fitted as $c_p = f(X, T)$ per dry mass of composite, with values between 1.1 and 3.0 kJ/(kg K) at 0 kg/kg, 30°C and 0.35 kg/kg, 90°C, respectively.

The macroporosity of the coating ε_P is estimated to 0.5, based on the composite dry density and the mass fractions and densities of the binder ($\rho = 1.1$ g/cm³, calculated from Kummer et al. [21] where the same octagonal stainless-steel masks were used) and the apparent dry density of the aluminium fumarate crystals. As reported measurements of the latter are lacking, it was estimated based on the structural data obtained by Alvarez et al. [19] by Rietveld refinement. They estimated the volume of a fully hydrated unit cell, consisting of four metal Al(OH) octahedrals ($m = 4 \cdot 44.0$ u) and four fumarate $C_4O_4H_2$ linkers ($m = 4 \cdot 114.1$ u), as 990 Å³, yielding $\rho = 1.06$ g/cm³. It should be noted that this value does not account for water-induced shrinking or swelling, nor for any defects or impurities that are likely to be found in the actual adsorbent particles.

The particle size of the initial adsorbent powder was measured at 18 µm, on average (Fig. S1).

2.2. Apparatus

Frequency response (FR) measurements are done with a custom setup detailed earlier (Fig. 1, Table 1) [18]. In addition, this setup allows large temperature jump (LTJ), large pressure jump (LPJ) and small pressure jump (SPJ) experiments with water [22–24].

The setup can be classified as a volume swing thermal FR inspired by approaches from other authors [13,25–28] but extended by a thorough control of the sample's thermal contact and a temperature response measurement in order to discriminate between heat and mass transfer effects. To our knowledge, comparable measurements have only been published by LIMSI-CNRS in the late 1990s [16,17,29] but with immense efforts regarding temperature measurements (liquid helium-cooled detector) to reach an NETD of 1.5–15 mK at 5 ms response time. Here, an off-the-shelf temperature sensor is employed at the expense of an up to two orders of magnitude higher noise level. The noise level is minimised by increasing the time constant for low frequencies of the sensor and compensated for by longer measurement times for higher frequencies, in order to reach satisfying precision.

Table 1
Principal characteristics of the measurement quantities; details have been published in [18]. Mean values of sample temperature and chamber pressure are obtained from slow and precise sensors (Pt100, MKS), whereas fast and less precise sensors (Heitronics, STS) are used for assessing frequency response values.

Quantity	Range	Typical uncertainty	Time constant	Device
Chamber volume	849–922 ml	0.4 ml (20°C), 1.3 ml (80°C)	1.3 ms	Schreiber Messtechnik LVDT
Chamber pressure slow	0–100 mbar	0.05 mbar (5 mbar), 0.15 mbar (100 mbar)	40 ms	MKS Baratron 627B
Chamber pressure fast	0–100 mbar	0.4 mbar (5 mbar, 30°C), 5 mbar (100 mbar, 60°C)	1 ms	STS ATM
Cold-plate temperature	20–95°C	0.1 K	~1 s	4-wired Pt100
Sample surface temperature	20–80°C	25 mK ($\tau = 1$ s) 1.1–0.6 K ($\tau = 5$ ms, 20–100°C)[1]	$\geq$ 5 ms (adjustable)	Heitronics KT15

[1] Noise equivalent temperature difference (NETD), depending on chosen time constant and measured temperature.

2.3. Procedure

The measurement procedure consists of three steps: (i) preconditioning to the desired state, (ii) determination of the equilibrium slopes and (iii) the actual FR measurement. Throughout the measurement, the temperature-controlled cabinet is kept at the measurement mean temperature T_0. Measurements are carried out at 30–60°C and in the entire loading range.

Pre-conditioning includes desorption at $p < 0.01$ mbar and 95°C overnight and dosing vapour from a calibrated volume to the actual loading X_0. The local slopes of the isotherm and isobar are determined with small volume and temperature variations, respectively. The latter also serves to exclude local hysteresis in the sorption equilibrium by comparing the loading reached at V_0 and T_0 coming from above and from below. Details are given elsewhere [18].

The FR measurement consists of a set of single-frequency sinusoidal excitations of the measurement chamber volume spaced in an (almost) geometric sequence between 10^{-3} and 5 Hz. This is realised by rotating the stepper motor with constant velocity, which is converted into a sinusoidal linear motion of the bellow through a specially designed cam. The stepper motor is controlled with the same DAQ device (Keysight U2351A) that records the bellow position, chamber pressure and sample surface temperature so that data acquisition and volume excitation are synchronised. The single-frequency sinusoidals are chosen for the straightforward implementation and as the most robust excitation signal. The signal-to-noise ratio is maximised by concentrating the whole signal power to a single frequency [30]. The number of periods is increased with the frequency to compensate for the reducing signal-to-noise ratio.

2.4. Data processing

Signals from sensors for bellow position, chamber pressure and sample surface temperature are recorded with a Keysight U2351A at a sampling rate of 10 kHz and 16-bit resolution. During measurement, data is down-sampled by integer averaging to a sampling rate of 1000 times the bellow frequency. This results in lower noise levels for lower bellow frequencies and a considerably reduced amount of raw data while the filter disturbance on the signal remains negligible. The complex responses $\tilde{V}$, $\tilde{p}$ and $\tilde{T}$ at the known bellow frequency f are obtained from the fast Fourier transformation (FFT) implemented in R [31]. Spectral leakage is avoided by carefully choosing bellow frequencies that allow for an integer amount of (averaged) samples per bellow period and cutting time series data to multiples of complete bellow periods. From a complex response $\tilde{y}$, the signal in the time domain can be reconstructed as

$$y(t) - y_0 = A_y \sin(2\pi f + \phi_y) \tag{1}$$

where $A_y = |\tilde{y}|$ is the signal amplitude and $\phi_y = \arg(\tilde{y})$ is the phase shift. $\tilde{y}$ can also be considered as a real 2-dimensional vector of $\mathrm{Re}(\tilde{y})$ and $\mathrm{Im}(\tilde{y})$, which is less intuitive but more convenient for further data processing as they are both $\in \mathbb{R}$, compared to $|\tilde{y}|$ (≥ 0) and $\arg(\tilde{y})$ ($\in [0,\ 2\pi]$).

Corrections are applied to the volume perturbation and the FR signals of the sample surface temperature and the measurement chamber pressure, as detailed in the following.

Chamber volume and surface temperature are corrected for low pass filter effects of the sensors by applying an inverse low pass filter to the measured response. Cut-off frequencies are 800 Hz for the volume and 200 Hz for the temperature measurement. Thus, the effect, mainly affecting the phase shift, remains small even for the highest measurement frequency of 5 Hz. In addition, the IR temperature signal is corrected for linearity errors by comparing the difference of steady-state values from small jumps around T_0 to those measured by the Pt100 of the cold plate.

The pressure signal is typically corrected based on responses from blank measurements compared to the expected isothermal response according to the mass balance Eq. (6) with no sample ($m_s = 0$) [9,32,33]. This correction accounts for effects from non-isothermal compression, adsorption at the walls, heterogeneous pressure distribution and sensor damping. The pressure correction consists of a simple multiplication of the measured pressure response $\tilde{p}_{\mathrm{msr}}$ with a correction factor:

$$\tilde{p}_{\mathrm{cor}} = \psi\, \tilde{p}_{\mathrm{msr}}. \tag{2}$$

The pressure correction factor $\psi = -\frac{\tilde{V}}{V_0}\frac{p_0}{\tilde{p}_{\mathrm{cal}}}$, with the blank measurement result $\tilde{p}_{\mathrm{cal}}$, can be deduced from the chamber mass balance Eq. (8). Results for ψ from a wide range of temperatures, pressures and frequencies are fitted using a scaled and centred multivariate Kriging model with noisy observations implemented in R [34] to obtain a correction function covering the whole operational range of the setup. After correction, the non-idealities of the pressure response are below 2% of the relative pressure response $\tilde{p}/p_0$.

2.5. Uncertainty evaluation

Uncertainty analysis was carried out based on GUM [35], including the uncertainty from sample variance (type A) and uncertainties from imperfect calibration and correction (type B).

The uncertainty estimation for the complex responses is based on Monte Carlo experiments on measured noise from blank experiments with stopped motor (type A) and all type B uncertainties that affect linearity. As uncertainties affecting only the absolute value (like offsets) are irrelevant to the complex response, a much higher precision can be reached as compared to absolute mean values. Complex error propagation is carried out as a bivariate combination of real and imaginary part uncertainties; in contrast, a combination of modulus and argument uncertainties has a strong bias

for values close to $0+i0$ and is advised against [36]. Uncertainties are strongly dependent on the bellow frequency f, the number of periods evaluated and the actual measurement value. Typical values of real and imaginary parts are 0.1–5 µl for $\tilde{V}$, (0.5×10^{-3})–(5×10^{-3}) mbar for $\tilde{p}$ and 0.8–30 mK for $\tilde{T}$.

Other uncertainties of the setup were discussed before [18].

3. Modelling

Frequency response analysis is a model-based method for the determination of transport processes. The sorption kinetic models derived in the following are as essential as the actual measurement. Both are combined in the parameter identification procedure described at the end of this section.

3.1. Principal approach

The framework for FR modelling is mainly based on the transfer function approach suggested in [37]. The principal assumptions are:

1 Perturbations of the loading, pressure/concentration and temperature are sufficiently small to allow linearisation of all equations with constant coefficients. These coefficients are assumed local for the given mean state but may be different for different mean states, i.e. different experiments.
2 The pressure distribution in the chamber is uniform.
3 The temperature of the gas in the chamber is constant and equal to the temperature of the sample support.
4 Adsorption occurs only on the sample and not on the chamber walls.
5 The chamber contains a pure working fluid atmosphere (single-component adsorption).
6 The gas may be described as ideal gas, which is a very good approximation for water in the pressure (< 100 mbar) and temperature (20–100°C) region of interest here. In principle, the models can be extended by different equations of state that are locally linearised. This might be relevant, e.g., for high-temperature applications or working fluids operated in a higher pressure range like ammonia.

Non-ideal effects contradicting assumptions 2–4 are accounted for in the experiments applying a pressure correction (see 2.4).

The mass balance of the measurement chamber is

$$0 = \frac{\mathrm{d}\bar{X}}{\mathrm{d}t} m_\mathrm{s} + \frac{\mathrm{d}m_\mathrm{g}}{\mathrm{d}t} \tag{3}$$

where $\bar{X}$ denotes the average loading of the sample (mass of adsorbed working fluid per mass of dry adsorbent), m_s is the dry adsorbent mass, and m_g is the gas mass in the chamber. With the ideal gas law and constant gas temperature T_0, this becomes:

$$\begin{aligned} 0 &= \frac{\mathrm{d}\bar{X}}{\mathrm{d}t} m_\mathrm{s} + \frac{\frac{\mathrm{d}}{\mathrm{d}t}(p_\mathrm{ch} V)}{R_w T_0} \\ &= \frac{\mathrm{d}\bar{X}}{\mathrm{d}t} m_\mathrm{s} + \frac{1}{R_w T_0}\left(V \frac{\mathrm{d}p_\mathrm{ch}}{\mathrm{d}t} + p_\mathrm{ch} \frac{\mathrm{d}V}{\mathrm{d}t} \right). \end{aligned} \tag{4}$$

For convenience, the variables are transformed to deviations from the temporal mean with

$$\begin{aligned} \hat{X} &= X - X_0 \\ \hat{p} &= p - p_0 \\ \hat{c} &= c - c_0 \\ \hat{T} &= T - T_0 \end{aligned} \tag{5}$$

and Laplace transformed $(\tilde{X} = \mathcal{L}(\hat{X}))$. Thus, the Laplace-transformed mass balance is

$$0 = s\tilde{\bar{X}} m_\mathrm{s} + \frac{1}{R_w T_0}\left(V_0 s \tilde{p}_\mathrm{ch} + p_0 s \tilde{V} \right). \tag{6}$$

The mass balance can be explicitly solved for the complex pressure volume transfer function

$$\begin{aligned} G_{pV}(s) = \frac{\tilde{p}}{\tilde{\bar{V}}} &= -\left(\frac{\tilde{\bar{X}}}{\tilde{\bar{V}}} \frac{m_\mathrm{s} R_w T_0}{V_0} + \frac{p_0}{V_0} \right) \\ &= -\left(G_{XV}(s) \frac{m_\mathrm{s} R_w T_0}{V_0} + \frac{p_0}{V_0} \right). \end{aligned} \tag{7}$$

This allows calculating the pressure response directly from known constants and the loading volume transfer function $G_{XV}(s) = \frac{\tilde{\bar{X}}}{\tilde{V}}$.

For the overall energy balance of the sample, we basically use the same approach that was used before [32,37], assuming an effective heat transfer coefficient h between the coating, which has the temperature T_btm at the interface, and the support, which is constantly at the mean temperature T_0. Convective or radiative heat transfer at the adsorbent surface is neglected. The energy balance is then

$$m_\mathrm{s} c_p \frac{\mathrm{d}\bar{T}}{\mathrm{d}t} = m_\mathrm{s} \Delta h_\mathrm{s} \frac{\mathrm{d}\bar{X}}{\mathrm{d}t} - Ah(T_\mathrm{btm} - T_0) \tag{8}$$

with the adsorbent mass-specific heat capacity c_p, the enthalpy of adsorption Δh_s and the sample surface area A (i.e. the reference surface for h). Laplace transformation with deviation variables as above yields:

$$m_\mathrm{s} c_p s \tilde{\bar{T}} = m_\mathrm{s} \Delta h_\mathrm{s} s \tilde{\bar{X}} - Ah \tilde{T}_\mathrm{btm}. \tag{9}$$

For models assuming homogeneous temperature distribution, all temperatures are equal ($\tilde{T} = \tilde{\bar{T}} = \tilde{T}_\mathrm{btm}$) and Eq. (9) simplifies to the form used by Wang et al. [37], which can be directly solved for $\tilde{T}$ to formulate the temperature loading transfer function

$$G_{TX}(s) = \frac{\tilde{T}}{\tilde{\bar{X}}} = \frac{m_\mathrm{s} \Delta h_\mathrm{s} s}{m_\mathrm{s} c_p s + Ah}. \tag{10}$$

This is slightly different from the formulation used by Wang et al. [37], but it is more convenient for the calculation of the measured temperature and pressure responses directly from $G_{XV}(s)$:~

$$\tilde{T} = \underbrace{G_{TX}(s) G_{XV}(s)}_{G_{TV}(s)} \tilde{V} \tag{11}$$

$$\tilde{p} = -\left(G_{XV}(s) \frac{m_\mathrm{s} R_\mathrm{w} T_0}{V_0} + \frac{p_0}{V_0} \right) \tilde{V}. \tag{12}$$

In cases where the assumptions for Eq. (10) do not apply, a direct formulation for $G_{TV}(s)$ will be required and the reduction to a single transfer function $G_{XV}(s)$ is no longer possible.

$G_{XV}(s)$ (or $G_{pV}(s)$ and $G_{TV}(s)$) may be computed directly from constants (transport parameters as well as material and setup properties) and the complex variable s according to analytical model solutions from the following section. With $s = j2\pi f$, this allows calculating the pressure and temperature frequency responses, which can then be fitted to the experimental results.

3.2. Heat and mass transfer models

Analytical solutions in the form of complex transfer functions convertible to $G_{XV}(s)$ are available for two non-isothermal cases with different complexities in the mass transfer modelling [37]:

a) “0DHT_LDF”: lumped heat transfer + linear driving force (LDF),
b) “0DHT_miD_3D”: lumped heat transfer + micropore (loading-driven) diffusion in radially symmetric spheres (not applicable here).

For the modelling of macropore diffusion in even layers of adsorbent coating and intra-crystalline (micropore) diffusion in non-isotropic materials with a single preferred diffusion direction like

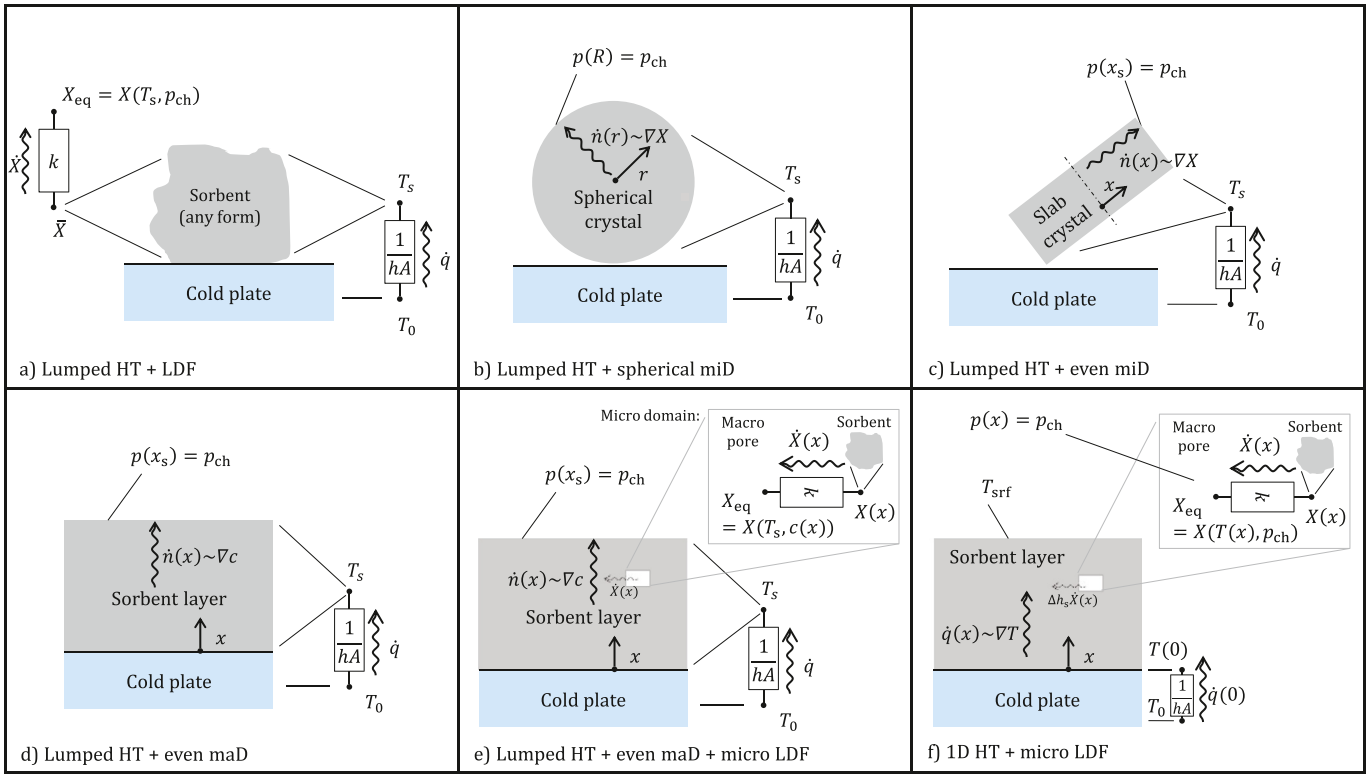

Fig. 2. Principles of different non-isothermal approaches to adsorption kinetic modelling with boundary conditions. FR solutions for (a) and (b) are available [37] in a similar formulation (c.f. S3), (c)–(d) are developed in this work (HT: heat transfer, miD: micro-diffusion, maD: macro-diffusion, LDF: linear driving force).

Table 2
Summary of FR model solutions developed in this work; details are given in the supplement as referenced.

Model	Loading volume transfer function $G_{XV}(S)$	Reference
c) Lumped HT + even miD	$-\frac{K_p p_0}{V_0}[\sqrt{\frac{s}{k_{mi}}}\coth(\sqrt{\frac{s}{k_{mi}}}) + \frac{m_s K_p R_w T_0}{V_0} - \frac{s}{\beta}]^{-1}$ with $k_{mi} = \frac{D_{mi}}{r^2}$ and $\beta = (Ah + c_p m_s s)/\Delta h_s K_T m_s$	S3.1
d) Lumped HT + even maD	$-\frac{K_p p_0}{V_0}[\sqrt{\frac{s}{k_{ma}}(1+\alpha)}(1 - \frac{s}{\beta(1+\alpha)})\coth(\sqrt{\frac{s}{k_{ma}}(1+\alpha)}) + \alpha(\frac{\varepsilon_p m_s}{\rho_s V_0} - \frac{s}{\beta(1+\alpha)})]^{-1}$ with $\alpha = K_p \rho_s R_w T_0/\varepsilon_p$, $k_{ma} = \frac{D_{ma}}{d^2}$ and β as above	S3.2
e) Lumped HT + even maD + micro-LDF	$-\frac{K_p p_0}{V_0}[\sqrt{\frac{s}{k_{ma}}\frac{\alpha+\gamma}{\gamma}}\ \gamma(1 - \frac{s}{\beta(\alpha+\gamma)})\coth(\sqrt{\frac{s}{k_{ma}}\frac{\alpha+\gamma}{\gamma}}) + \alpha(\frac{\varepsilon_p m_s}{\rho_s V_0} - \frac{s}{\beta(\alpha+\gamma)})]^{-1}$ with $\gamma = 1 + s/k_{LDF}$ and α, β, k_{ma} as above	S3.3
f) 1D HT + micro-LDF	$G_{XV}(s)$ is not useful in this case. $G_{pV}(s)$ and $G_{TV}(s)$ are given separately in the reference.	S3.4

aluminium fumarate [19,38], the diffusion equation needs to be solved on an even-plate or slab geometry. Moreover, to model the heat transfer effect of the coating thickness, a 1D heat transfer model with contact resistance is required.

For this work, we developed the FR solutions for differently simplified models (c.f. Fig. 2):

c) "0DHT_miD": lumped heat transfer with micropore diffusion on a slab geometry (homogeneous concentration in the macropores and homogeneous temperature in the coating),
d) "0DHT_maD": lumped heat transfer with macropore diffusion on a flat-plate geometry (homogeneous loading in the crystals and homogeneous temperature in the coating),
e) "0DHT_maD_LDF": lumped heat transfer with macropore diffusion combined with an LDF approach for micropore diffusion (homogeneous temperature in the coating)
f) "1DHT_miLDF": heat conduction in the coating with a thermal contact resistance to the support and with an LDF approach for micropore diffusion (homogeneous concentration in the macropores)

A computer algebra system (CAS) was used (Wolfram Mathematica® in our case) to efficiently solve the equation systems. The solutions are summarised in Table 2 and detailed in SI3.

In the last two models, the micropore diffusion is approximated with the LDF approach by analogy to the isothermal case with linearised equilibrium and homogeneous uptake distribution [39]:

$$D_{mi} \approx \frac{k_{LDF} r^2}{\sigma(\sigma+2)}, \tag{13}$$

where the curvature factor $\sigma = \frac{rA}{V} = 1$ for the even-plate geometry of the 1D channel structure of the aluminium fumarate crystals ($\sigma = 2$ for cylinder and $\sigma = 3$ for sphere geometries). r is the distance between the surface and the no-flux boundary, i.e. the particle radius here.

Simultaneous space discretisation of both heat and macropore diffusion could principally be solved analytically. However, the straightforward approach applied to the other cases fails to produce useful results and is thus omitted here – the solutions obtained by CAS are so fragmented and extensive that numerical evaluation runs into large rounding errors. These approaches are typically found as numerical non-linear models in the time domain [22,23,40]. Also non-straightforward CAS-based approaches as proposed earlier [41] might be useful here but are left for future studies.

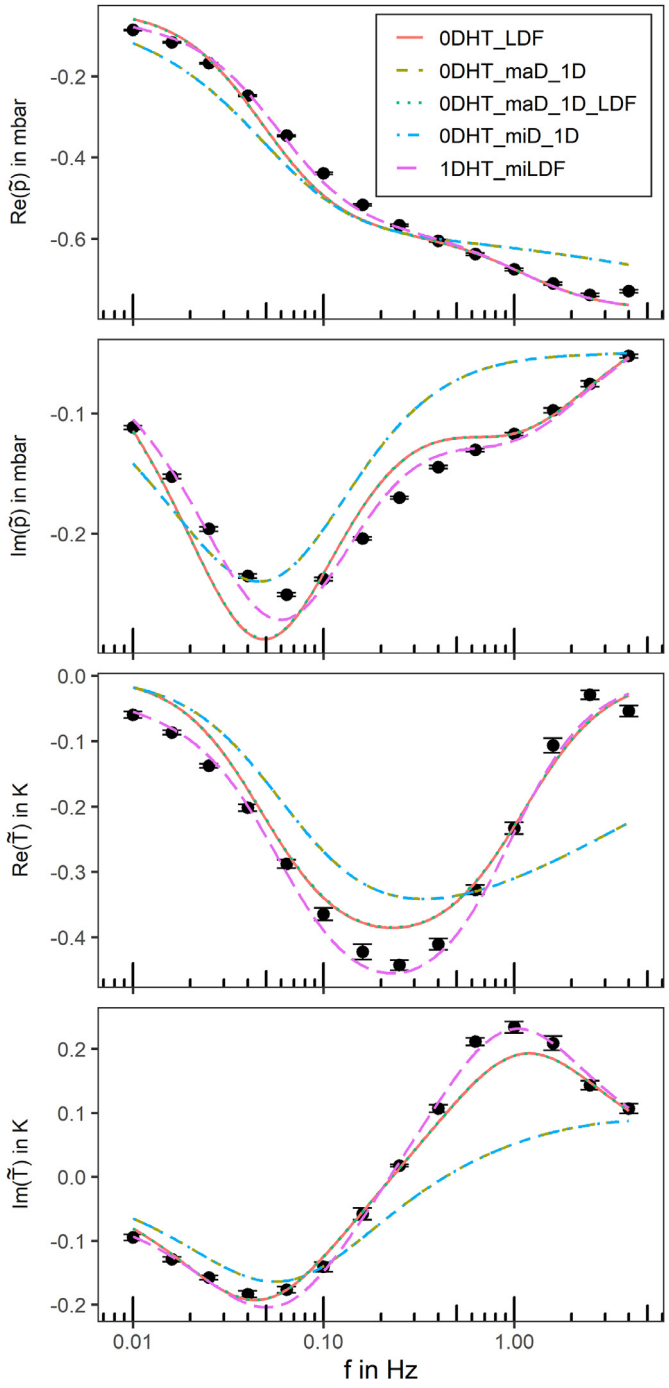

Fig. 3. Example for the measured frequency response of water on the sample Ct_610 at $p = 18.5$ mbar, $T = 40$°C and $X_{\text{eff}} = 0.09$ g/g in comparison to best-fit results of different models for a geometric sequence of 14 frequencies between 0.01 and 4 Hz, shown as non-normalized real and imaginary part of the complex deviation variables of the chamber pressure $\tilde{p}$ and the surface temperature $\tilde{T}$.

3.3. Parameter identification

Most model parameters can be determined externally (c.f. Section 2.1) or in the first part of the measurement procedure [18], whereas the parameters for heat and mass transfer are identified through a generalised weighted least-squares method. The best estimate for the parameter vector $\boldsymbol{P}$ (denoted as $\hat{\boldsymbol{P}}$) is gained by minimising the error functional $E(\boldsymbol{P})$. A confidence region is given around $\hat{\boldsymbol{P}}$ based on the contour of $E(\boldsymbol{P})$, following an approach from Marsili-Libelli [42]. The value of $E(\hat{\boldsymbol{P}})$ is an average relative deviation between the fitted model and the experiment. For further details, refer to S4 in the supplement.

4. Results

The results from the FR measurements (Fig. 3) show the typical bimodal shape indicating several distinct transfer processes at different characteristic frequencies. The signal-to-noise ratio is sufficient, and for lower frequencies, more than sufficient. This might allow further reduction of the measurement time, e.g. by replacing the single-frequency sinusoidal signal by a phase-shifted multisine with a high signal power, i.e. a low crest factor [30].

4.1. Model comparison

The measured FR (Fig. 3) shows the typical bimodal shape observed before for non-isothermal adsorption systems [16,32]. Note that here $\text{Im}(\tilde{p})$ and $\text{Im}(\tilde{T})$ are proportional to the negative "out-of-phase curves" due to different phase shift definitions. The maximum temperature amplitude is in the order of several 100 mK, which is typical of adsorption with water measured in our apparatus and allows for a good signal-to-noise ratio, and is about one order of magnitude higher than the values reported by Bourdin et al. [16].

For the example shown in Fig. 3, the simple macro- and micropore diffusion models 0DHT_maD and 0DHT_miD fail to represent the experimental data (weighted residual error $E(\hat{\boldsymbol{P}}) = 0.20$). Due to the mathematically similar structure, both models yield the same best-fit shape for all measurements. As the mismatch is observed throughout all experiments, both models will be disregarded in the following. A better fit ($E(\hat{\boldsymbol{P}}) = 0.08$) is achieved with the macropore diffusion + micro-LDF model (0DHT_maD_LDF). However, the best fit ($E(\hat{\boldsymbol{P}}) = 0.04$) results when discretising the heat transfer with the 1DHT_miLDF model. The simple 0DHT_LDF model returns the same fit result as 0DHT_maD_LDF, indicating that the macropore diffusion is not relevant to the example shown. For a similar reason, the 0DHT_LDF model converges toward the results from the 1DHT_miLDF model when fitting other experiments: For large values of λ (small Biot numbers), the solution of the 1DHT_miLDF model simplifies to that of the 0HT_LDF model, as the temperature distribution becomes homogeneous. Therefore, and for its limited information content, the 0HT_LDF is disregarded in the following.

Further assessment shows that the model 1DHT_miLDF is more appropriate than the model 0DHT_maD_LDF to plausibly represent the observed behaviour of all measurements. To this end, both models are further analysed looking at two aspects: the relative residual error $E(\hat{\boldsymbol{P}})$ (Fig. 4, Fig. S2) and the identified parameters $\hat{\boldsymbol{P}}$ (Fig. 5). Starting with $E(\hat{\boldsymbol{P}})$, the overall best-fitting model is 1DHT_miLDF (Fig. S2). Furthermore, with the sample layer thickness, the residual error $E(\hat{\boldsymbol{P}})$ rises for 0DHT_maD_LDF and drops for 1DHT_miLDF (Fig. 4). The difference between the two models lies in whether the heat conduction or the macropore diffusion is the dominant transport mechanism perpendicular to the coating layer. This becomes more relevant in the case of thicker coatings, indicating that the heat transport discretisation (1DHT_miLDF) is more relevant to catch the overall behaviour.

The second aspect, the identified transport parameters (Fig. 5), supports this hypothesis by showing plausible results only for 1DHT_miLDF. Distributed transport parameters like diffusivities and thermal conductivity should not be dependent on the coating thickness. However, for the 0DHT_maD_LDF model, a coating thickness dependency is found for all parameters, whereas it is only plausible for the overall heat transfer coefficient h to drop with rising coating thickness; k_{LDF} and D_{ma} should be independent of the

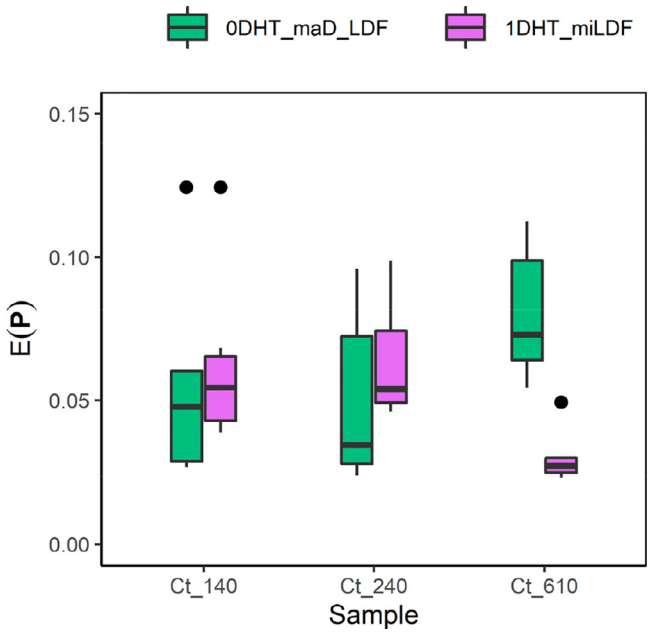

Fig. 4. Residual error, i.e. $E(\hat{P})$, for the two best-fitting models over the coating thickness.

thickness, as all samples have the same composition. D_{ma} is expected to rise with the pressure, but it shows a U-shaped loading dependency, which is not plausible. The heat transfer coefficient is expected to depend on the pressure and the grain-grain contact properties, but it also shows a slightly chaotic U-shape-like loading dependency, which is not plausible. For the 1DHT_LDF model, a coating-thickness-independent U-shaped loading dependency is found for the microdiffusivity, i.e. the transport diffusivity, which can plausibly be explained by the strong change of the thermodynamic factor, as we will discuss later. Yet, the two heat transfer-related parameters, λ and h, are fluctuating arbitrarily by orders of magnitude for the thinner samples. Only fits to measurements of the thickest sample yield a plausible thermal conductivity in the order of 0.1 W/(m K), independent of the loading. In the following, the evaluation will thus focus on the 1HT_miLDF model.

4.2. Identified transport parameters

Based on the model with discretised heat transfer and LDF-simplified micropore diffusion (1DHT_miLDF), the thermal conductivity λ of the samples was identified as about 0.07 W/(m K). At 40°C, values for k_{LDF} are between 0.1 and 3 s^{-1}, leading to an LDF-approximated micropore transport diffusivity D_{mi} between 3×10^{-12} and 1×10^{-10} m^2/s with a characteristically U-shaped loading dependency (Fig. 8). The heat transfer coefficient h for the contact between coating and support was identified as $\geq 4 \times 10^3$ W/(m^2K). An upper boundary for h cannot be given, as it proved to be irrelevant to the overall transport process (non-identifiable). Details will be discussed in the following.

The sensitivity of the individual fit results to h is extremely low (Fig. S3). For the thinner samples, any combination of λ and h resulting in the same total heat transfer resistance yields similar values of the error functional, whereas for the thicker sample, only high enough values of h yield good fits. This explains the arbitrary oscillation of λ and h for Ct_240 in Fig. 5: The fitting algorithm will arbitrarily return any value along the long stretched minimum "valley" of $E(\boldsymbol{P})$. As λ, h and D_{mi} should be equal for all samples and to increase the power of the parameter identification procedure, the fit procedure was applied to find a single set of parameters fitting well to multiple samples ("multi-fit"). For this, experimental results from all three samples were pooled for similar X, T-states and fitted to a single $\boldsymbol{P}$ while all other specific model parameters were kept at the precise state of each individual measurement and sample. The contour plot of $E(\boldsymbol{P})$ in the $\hat{D}_{mi}$ plane (Fig. 6) reveals that values below 4×10^3 W/(m^2K) are unlikely for h, but no upper boundary can be given.

In the following, we will therefore present the model results based on an ideal (i.e. non-limiting) thermal contact (i.e. $h \to \infty$). As the values obtained for λ rise with decreasing h, this approach yields conservative estimates for λ. In the case analysed in Fig. 6, this leads to a maximum underestimation of less than 0.02 W/(m K) within the standard confidence level.

For the ideal contact model, the form of the confidence limit of D_{mi} and λ shows that the two variables can be distinguished clearly (Fig. 7). The maximal extent of the standard confidence region as depicted will be used as a definition for error bars in the other plots. A three-dimensional evaluation of the standard confidence region is possible in principle but omitted here for computational constraints and limited insight gain.

The parameter values identified with the ideal contact model do not show any significant dependency on the coating thickness (Fig. 8). The thermal conductivity of the coating is found to be constant throughout all measurement points, with values around 0.07 W/(m K), which seems plausible if compared to, e.g., the true thermal conductivity of 0.14–0.2 W/(m K) found for silica gels [43,44]. It can be expected that the thermal conductivity is lower for the porous coating than for the pure adsorbent, due to contact resistances and increased path lengths. The missing loading and pressure dependency that one might expect, and which was reported before for, e.g., granular beds of silica gel/water [45], could be explained by a heat transfer limited by binder/adsorbent contact resistances and conduction in the binder and/or the gas phase. The – possibly loading dependent – thermal conductivity of the adsorbent crystal would just add a low conductive resistance in series. Assuming macropores in the order of the adsorbent particles ($d = 18$ µm), the inverse Knudsen number under experimental conditions is in the order of 5–25, which leads to only minor deviations from the (pressure-independent) gas phase thermal conductivity [46]. Given that the macropore diffusion is not limiting the overall dynamics, the thermal conductivity might be worth addressing by, e.g., densifying the coating. The results for micro-transport diffusivity D_{mi} hardly differ from the non-idealised model (Fig. 5). The pronounced loading dependency of D_{mi} might be explained with the Darken factor as detailed in the following section.

4.3. Interpretation of micropore mass transfer

Tentatively, the adsorbate diffusivity D_{ad}, i.e. the self-diffusivity, may be calculated from the LDF-approximated micropore transport diffusivity D_{mi} taking into account the Darken factor $\frac{\mathrm{d}\ln p}{\mathrm{d}\ln X}$ (also referred to as thermodynamic factor) [47]:

$$D_{ad} = D_{mi}\frac{\mathrm{d}\ln X}{\mathrm{d}\ln p} = D_{mi}\frac{\mathrm{d}X}{\mathrm{d}p}\frac{p_0}{X_0}. \quad (14)$$

This correction compensates for most of the loading dependency observed for the transport diffusivity D_{mi} with values for D_{ad} of about 1×10^{-11} m^2/s at 40°C (Fig. 9). Pulsed-field gradient nuclear magnetic resonance (PFG NMR) measurements of water in saturated aluminium fumarate at 25°C yielded self-diffusivities of $D_{\parallel} = (6.0 \pm 0.4) \times 10^{-10}$ m^2/s and $D_{\perp} = (5.0 \pm 0.4) \times 10^{-12}$ m^2/s for the diffusion in the direction of the 1D channels and perpendicular to them [38], while the overall diffusion is dominated by $D_{\parallel}$. Our estimate of D_{ad} directly depends on our assumptions of

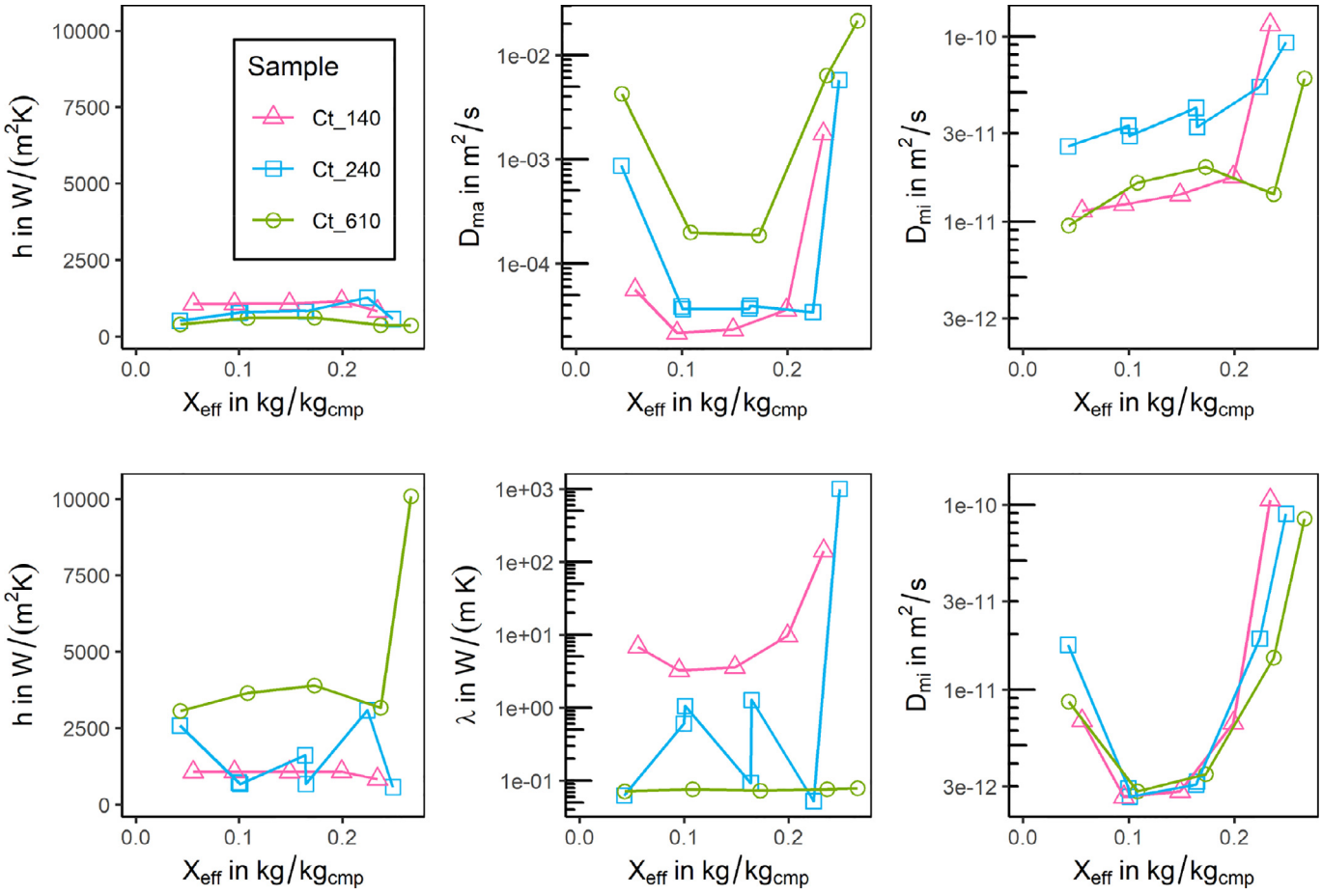

Fig. 5. Identified parameters using different models (upper panels: 0DHT_maD_LDF; lower panels: 1DHT_miLDF) over the effective loading for 40°C and different coating thicknesses (different colours and symbols); the LDF parameter $\boldsymbol{k_{LDF}}$ is expressed as the micropore transport diffusivity $\boldsymbol{D_{mi}}$ according to Eq. (13). Lines are only meant as guides to the eye.

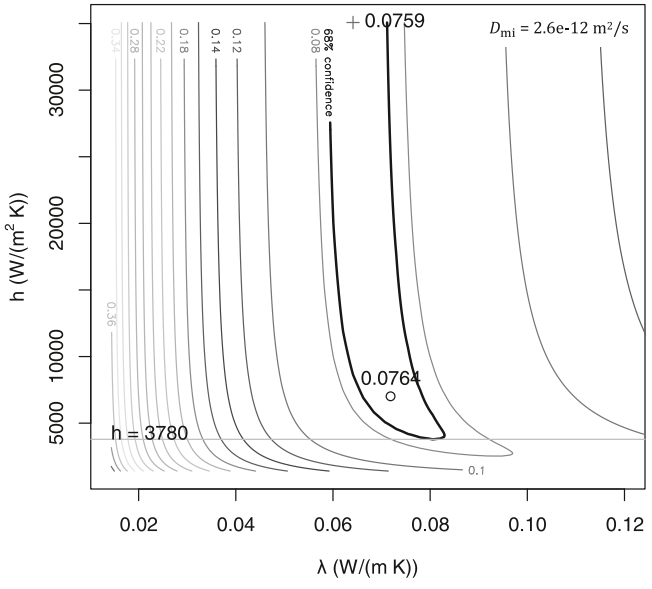

Fig. 6. Contour plot of $E(P)$ over λ and h for the simultaneous fit of measurement results of the three samples (Ct140, Ct240, Ct610) under similar conditions ($X_{0,\mathrm{eff}} \approx 0.16$ g/g, $T_0 = 40$°C, $p_0 \approx 20.7$ mbar) to the model 1DHT_miLDF with D_{mi} fixed at the best estimate (2.6×10^{-12} m^2/s). Open circle: minimum found by the fitting algorithm; red cross: minimum found by parameter variation for creating this plot; bold line: standard confidence limit (c.f. Eq. (S27)).

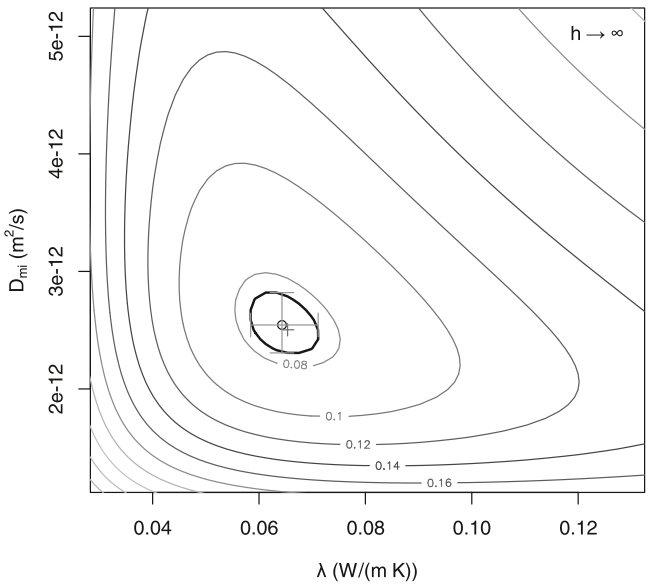

Fig. 7. Contour plot of $E(P)$ for the same fit as in Fig. 6 but over D_{mi} and λ for model 1DHT_miLDF with ideal thermal contact ($h \to \infty$). Bold line: standard (68%) confidence limit; error bars depict the definition confidence limits used in the other plots; open circle: minimum found by the fitting algorithm; red cross: minimum found by parameter variation for creating this plot.

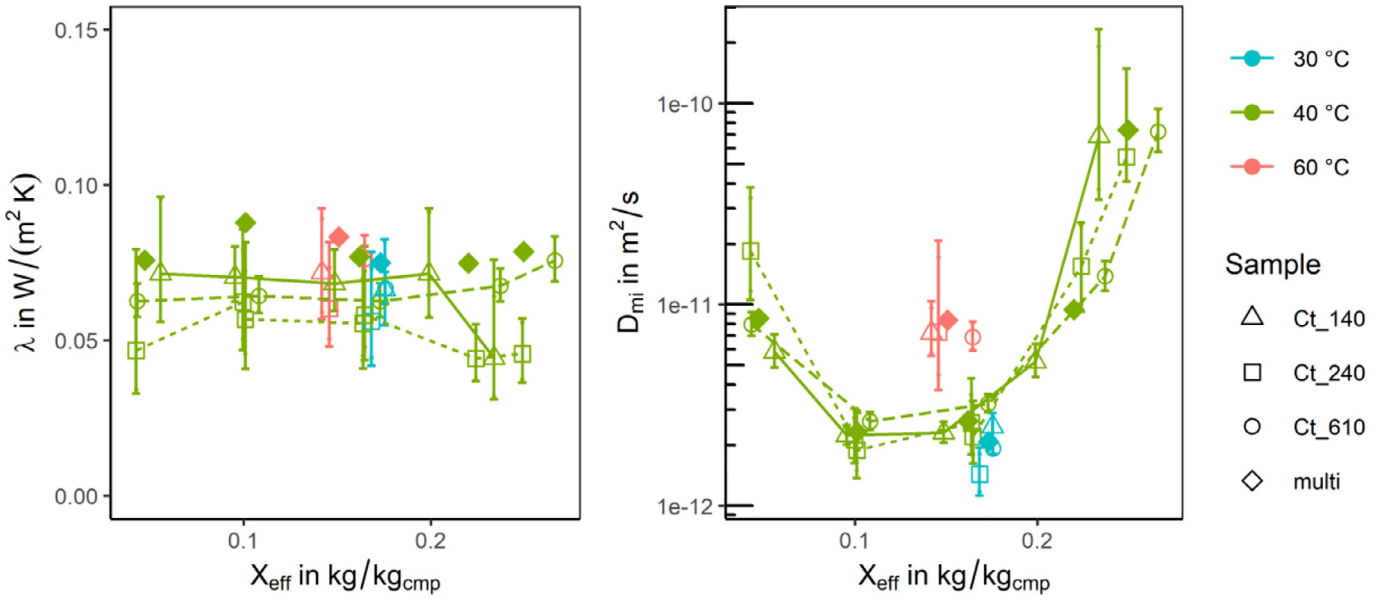

Fig. 8. Estimated parameters from the model 1DHT_miLDF with ideal thermal contact between support and coating for different coating thicknesses over the effective loading. "multi" (filled symbols) indicates results from simultaneous fit of all samples for similar X, T conditions with non-ideal thermal contact. Lines are only meant as guides to the eye.

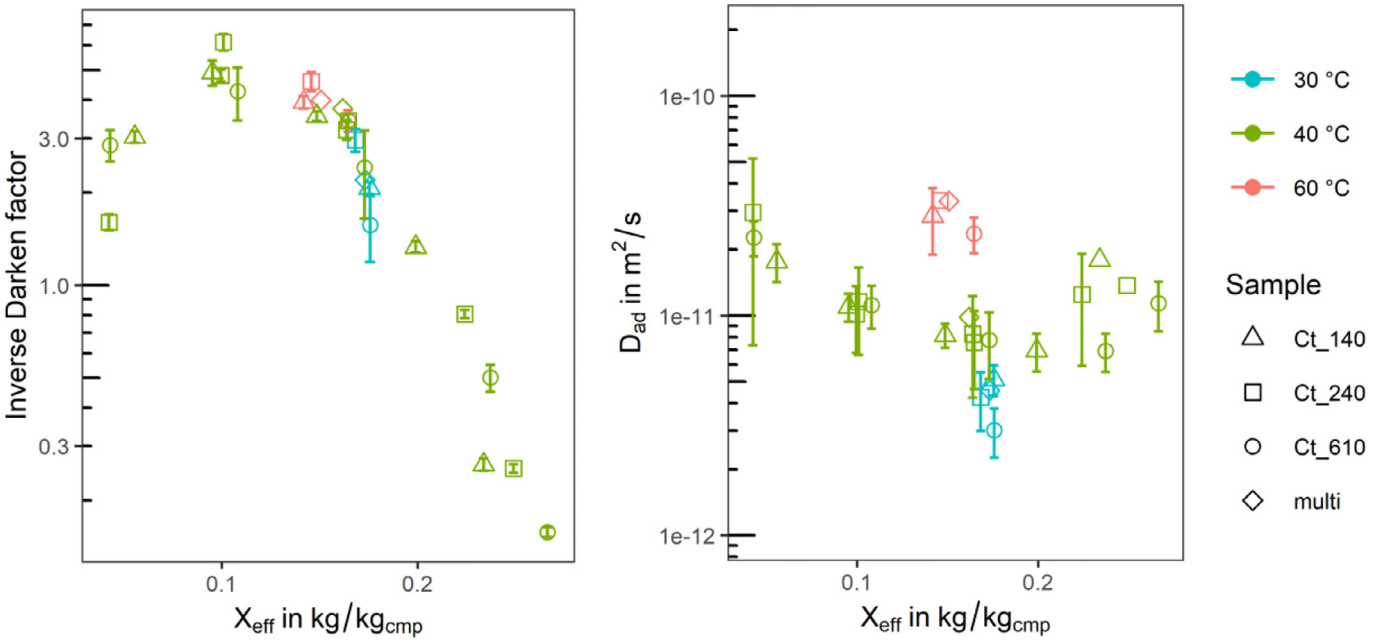

Fig. 9. Inverse Darken factor calculated from measured absolute and differential equilibria [18] and adsorbate diffusivity calculated from the identified micro-transport diffusivity (Fig. 8).

the validity of the LDF approximation, c.f. Eq. (13), and the diffusion path length. However, a wrong diffusion path length is not able to explain the discrepancy of about two orders of magnitude between our D_{ad} and the PFG NMR $D_{||}$: The diffusion path length of the micropore diffusion, i.e. the length from the particle surface to its centre, would need to be in the order of 100 µm, which is impossible given the measured adsorbent particle size being in the order of 18 µm (Supplementary Information S2). It seems more likely that deriving a micropore diffusion coefficient from k_{LDF} (LDF approximation) is misleading here. While the LDF model reproduces the experimental FR results particularly well, k_{LDF} might have a different physical meaning, e.g. a mass transfer barrier of unknown nature. This remains an open question to be further investigated, which, however, does not affect the quality of the description of the macroscopic processes, as we will show in the next section.

Irrespective of the physical interpretation, the data allows an Arrhenius plot of points with similar loading $X_{eff} \approx 0.15$ g/g (Fig. 10). It shows the linear form of the inverse temperature dependency expected:

$$\ln D_{ad} = \ln D_{ad,0} - \frac{E_a}{RT} \tag{15}$$

with the activation energy $E_a = 55.0 \pm 3.1$ kJ/mol.

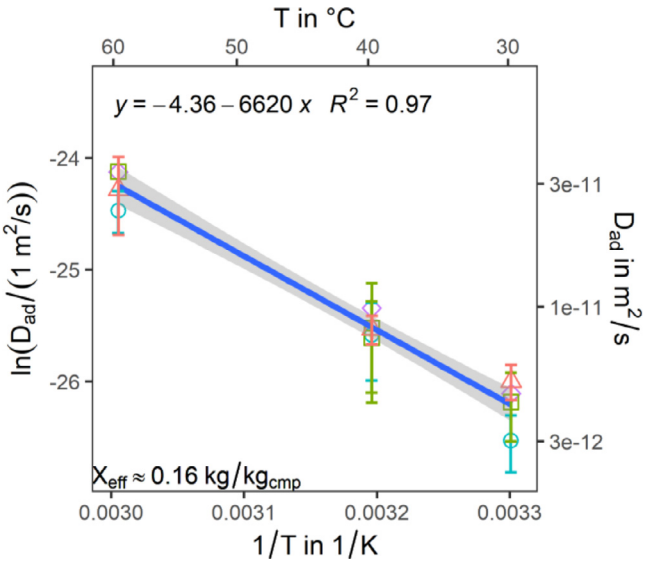

Fig. 10. Arrhenius plot of the adsorbate (self) diffusion of water in aluminium fumarate with linear fit and standard error (blue line, grey area) for points with similar loading ($X_{eff} = 0.16 \pm 0.02$ kg/kg$_{cmp}$) of all three coating thicknesses evaluated; the fit refers to the bottom and left axes.

4.4. Model validation with LTJ results

The identified transport and thermodynamic parameters were used for a non-linear simulation of an LTJ response, using an existing implementation of the 1DHT_miLDF model (Fig. 2f) in the time domain [22]. The results are compared to earlier experimental results on the same samples [48]. The simulation is based on loading- and temperature-dependent microdiffusivity, constant thermal conductivity (see Section 4.2), constant adsorption enthalpy and the fitted adsorption equilibrium as identified before [18]. Details of the parametrisation are given in the Supplementary Information S6. The simulation is solely based on parameters identified by FRA, without any fitting in the time domain.

The results show very good agreement (Fig. 11), validating the aforementioned procedures and identification results. The deviation between measurement and simulation show an improvement compared to previous works where similar transport models were fitted directly in the time domain [22,49]. Our results indicate that the deviation observed before was rather due to the incompletely mapped state dependency of the transfer coefficients and not due to the general model simplification like the reduction of particle size and layer thickness distributions to single values.

5. Conclusion

In this work, we developed and validated a method for local (in the thermodynamic state space) measurements of the sorption dynamics based on FRA. Combined with linearised heat and mass transfer models in the Laplace domain, physical transport coefficients can be determined. These coefficients, with their state dependency, allow precise non-linear modelling of application-relevant processes in the time domain. As these models are explicitly including geometrical parameters, they may be directly used for the design and optimisation of Ad-HX. In particular, a model was developed that takes the spatial temperature distribution into account.

The measurement procedure was developed further so that the information required for the models on (a) sorption equilibria and (b) sorption enthalpies can be determined in the same measurement sequence under exactly the same conditions. The only quantity required from external sources is the heat capacity of the sample for all thermodynamic states of interest. Literature on the heat capacity of sorption materials, especially as a function of the loading, is scarce and direct measurements are costly. Thus, its inclusion in our measurement procedure should be aimed at in future research.

Samples coated with a composite of aluminium fumarate particles with Silres® as a binder in different thicknesses (140–610 µm) were examined extensively with this method at 30–60°C and in the entire loading range. The relevant transport mechanisms are heat transfer by conduction in the coating layer (0.07 W/mK) and mass transfer into the particles. The latter was successfully described with an LDF approach. The LDF time constant showed a pronounced temperature and loading dependency, which could be described by interpreting the mass transfer as a micropore diffusion process. While the actual physical nature of the mass transport process at the micro-level remains an open question, the macroscopic dynamics can be predicted with high precision in a large range of operational conditions. The thermal contact resis-

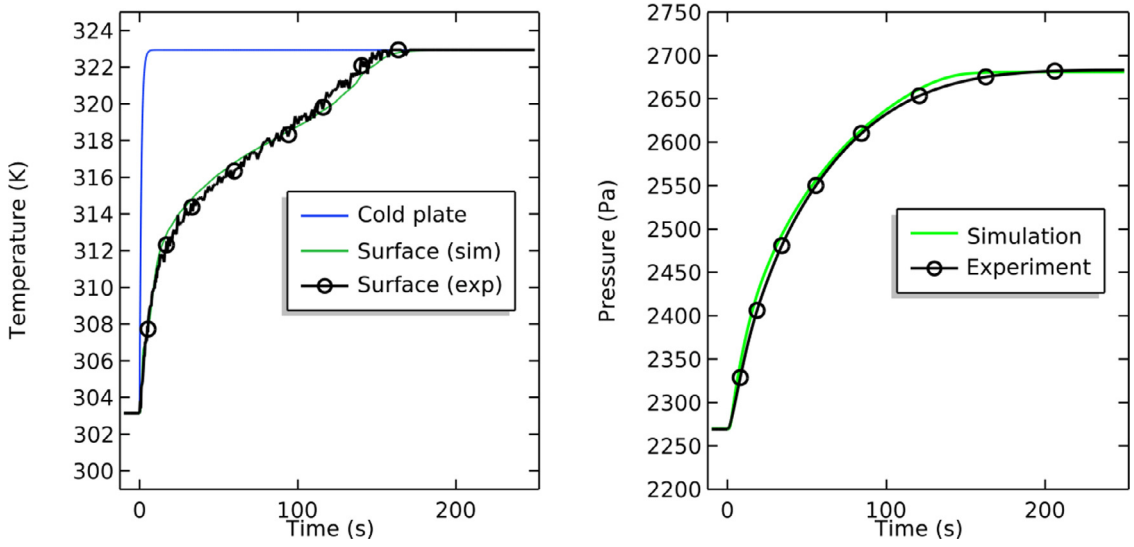

Fig. 11. Response of the surface temperature (left) and the chamber pressure (right) to a large jump of the cold-plate temperature (desorption) measured for sample Ct_610 and simulated with the T, X-dependent transport and equilibrium parameters identified in this work.

tance between support and coating as well as the macro-diffusion between the particles in the coating layer were found to be of minor relevance to the overall sorption dynamics.

The samples showed a generally high performance. Due to the sorption equilibrium of aluminium fumarate, this performance can be achieved under very favourable temperature conditions with low driving temperature. Further improvement is expected by more compact coatings with smaller adsorbent particles.

Author contributions

E.L. developed and designed the FR measurement apparatus, performed the measurements, processed the data, developed and solved the mathematical models and drafted the manuscript. The FR apparatus is an extension to a setup developed by A.V., G.F. and L.S.; G.F., L.S. and G.S. supervised continuously the PhD project of E.L.; A.V. designed the LTJ experiment and performed the nonlinear numerical simulations for result validation. All authors supported the writing process with several internal reviews.

Credit author statement

Eric Laurenz: Conceptualization, Methodology, Software, Formal analysis, Investigation, Resources, Data curation, Writing – Original draft preparation, Visualization, Funding acquisition; **Gerrit Füldner:** Conceptualization, Validation, Writing – Review and editing, Supervision, Project administration, Funding acquisition; **Andreas Velte:** Formal analysis, Validation, Writing – Review and editing, Visualization; **Lena Schnabel:** Validation, Writing – Review and editing, Supervision, Funding acquisition; **Gerhard Schmitz:** Writing – Review and editing, Supervision, Funding acquisition

Declaration of Competing Interest

The authors declare that they have no known competing financial interests or personal relationships that could have appeared to influence the work reported in this paper.

Acknowledgments

The authors would like to thank Harry Kummer for particle size distribution measurements and supervising the sample preparation, Raffael Wolf for carrying out the sample preparation, and Florian Tönnies for implementing parts of the data processing program. This work resulted widely from the PhD project of Eric Laurenz for which funding by Heinrich Böll Stiftung is gratefully acknowledged. In addition, funding by BMBF for project WasserMod2 (FKZ 03ET1554A) is gratefully acknowledged.

Supplementary materials

Supplementary material associated with this article can be found, in the online version, at doi:10.1016/j.ijheatmasstransfer.2021.120921.

References

[1] F. Meunier, Adsorption heat powered heat pumps, Appl. Therm. Eng. 61 (2013) 830–836.
[2] Y.I. Aristov, Adsorptive transformation and storage of renewable heat: Review of current trends in adsorption dynamics, Renewable Energy 110 (2017) 105–114.
[3] D. Lenzen, J. Zhao, S.-J. Ernst, M. Wahiduzzaman, A. Ken Inge, D. Fröhlich, H. Xu, H.-J. Bart, C. Janiak, S. Henninger, G. Maurin, X. Zou, N. Stock, A metal-organic framework for efficient water-based ultra-low-temperature-driven cooling, Nat. Commun. 10 (2019) 3025.
[4] T. Wilde, M. Ott, A. Auweter, I. Meijer, P. Ruch, M. Hilger, S. Kuhnert, H. Huber, in: CooLMUC-2: a supercomputing cluster with heat recovery for adsorption cooling, 2017, pp. 115–121. Proceedings.
[5] L. Schnabel, G. Füldner, A. Velte, E. Laurenz, P. Bendix, H. Kummer, U. Wittstadt, Innovative adsorbent heat exchangers: design and evaluation, in: H.-J. Bart, S. Scholl (Eds.), **Innovative Heat Exchangers**, Springer International Publishing, Cham, 2018, pp. 363–394.
[6] A. Freni, B. Dawoud, L. Bonaccorsi, S. Chmielewski, A. Frazzica, L. Calabrese, G. Restuccia, Adsorption Heat Exchangers, in: A. Freni (Ed.), **Characterization of zeolite-based coatings for adsorption heat pumps**, Springer, Cham, 2015, pp. 35–53.
[7] S. Graf, S. Eibel, F. Lanzerath, A. Bardow, Validated performance prediction of adsorption chillers: bridging the gap from gram-scale experiments to full-scale chillers, Energy Technol (2020) 1901130.
[8] L.M. Naphtali, L.M. Polinski, A novel technique for characterization of adsorption rates on heterogeneous surfaces, J. Phys. Chem. 67 (1963) 369–375.
[9] Y. Yasuda, Determination of vapor diffusion coefficients in zeolite by the frequency response method, J. Phys. Chem. 86 (1982) 1913–1917.
[10] E. Iglesia, S.C. Reyes, Frequency Response Techniques for the Characterization of Porous Catalytic Solids, in: J.J. Spivey, S.K. Agarwal, H.H. Kung (Eds.), Catalysis, Specialist Periodical Reports, Royal Society of Chemistry, Cambridge, 1994.
[11] L.M. Sun, F. Meunier, P. Grenier, D.M. Ruthven, Frequency response for non-isothermal adsorption in biporous pellets, Chem. Eng. Sci. 49 (1994) 373–381.
[12] B.K. Sward, M.D. LeVan, Frequency response method for measuring mass transfer rates in adsorbents via pressure perturbation, Adsorption 9 (2003) 37–54.
[13] L. Song, L.V.C. Rees, Frequency Response Measurements Of Diffusion In Microporous Materials, in: H.G. Karge, J. Weitkamp (Eds.), **Adsorption and diffusion**, Springer, Berlin, 2008, pp. 235–276.
[14] T.J. Giesy, Y. Wang, M.D. LeVan, Measurement of mass transfer rates in adsorbents: new combined-technique frequency response apparatus and application to CO2 in 13X Zeolite, Ind. Eng. Chem. Res. 51 (2012) 11509–11517.
[15] L.M. Sun, F. Meunier, J. Kärger, On the heat effect in measurements of sorption kinetics by the frequency response method, Chem. Eng. Sci. 48 (1993) 715–722.
[16] V. Bourdin, P. Grenier, F. Meunier, L.M. Sun, Thermal frequency response method for the study of mass-transfer kinetics in adsorbents, AIChE J. 42 (1996) 700–712.
[17] V. Bourdin, A. Germanus, P. Grenier, J. Kärger, Application of the thermal frequency response method and of pulsed field gradient NMR to study water diffusion in zeolite NaX, Adsorption 2 (1996) 205–216.
[18] E. Laurenz, G. Füldner, L. Schnabel, G. Schmitz, A novel approach for the determination of sorption equilibria and sorption enthalpy used for mof aluminium fumarate with water, Energies 13 (2020) 3003.
[19] E. Alvarez, N. Guillou, C. Martineau, B. Bueken, B. Van de Voorde, C.Le Guillouzer, P. Fabry, F. Nouar, F. Taulelle, D. de Vos, J.-S. Chang, K.H. Cho, N. Ramsahye, T. Devic, M. Daturi, G. Maurin, C. Serre, The structure of the aluminum fumarate metal-organic framework A520, Angew. Chem. Int. Ed. 54 (2015) 3664–3668.
[20] C. Kiener, U. Müller, M. Schubert, WO/2007/118841, 2009.
[21] H. Kummer, M. Baumgartner, P. Hügenell, D. Fröhlich, S.K. Henninger, R. Gläser, Thermally driven refrigeration by methanol adsorption on coatings of HKUST-1 and MIL-101(Cr), Appl. Therm. Eng. 117 (2017) 689–697.
[22] A. Velte, G. Füldner, E. Laurenz, L. Schnabel, Advanced Measurement and Simulation Procedure for the Identification of Heat and Mass Transfer Parameters in Dynamic Adsorption Experiments, Energies 10 (2017) 1130.
[23] G. Füldner, **Stofftransport und Adsorptionskinetik in porösen Adsorbenskompositen für Wärmetransformationsanwendungen**, Universiät Freiburg, Freiburg, 2015.
[24] L. Schnabel, **Experimentelle und numerische Untersuchung der Adsorptionskinetik von Wasser an Adsorbens-Metallverbundstrukturen**, TU Berlin, Berlin, 2009.
[25] M.D. Turner, L. Capron, R.L. Laurence, W.C. Conner, The design and construction of a frequency response apparatus to investigate diffusion in zeolites, Rev. Sci. Instrum. 72 (2001) 4424–4433.
[26] D. Shen, L.V.C. Rees, Study of fast diffusion in zeolites using a higher harmonic frequency response method, J. Chem. Soc. Faraday Trans. 90 (1994) 3011–3015.
[27] S.C. Reyes, J.H. Sinfelt, G.J. DeMartin, R.H. Ernst, E. Iglesia, Frequency modulation methods for diffusion and adsorption measurements in porous solids, J. Phys. Chem. B 101 (1997) 614–622.
[28] Mohammad Iftekhar Hossain, **Volume Swing Frequency Response Method For Determining Mass Transfer Mechanisms in Microporous Adsorbents**, University of South Carolina - Columbia, 2014.
[29] V. Bourdin, P.G. Gray, P. Grenier, M.F. Terrier, An apparatus for adsorption dynamics studies using infrared measurement of the adsorbent temperature, Rev. Sci. Instrum. 69 (1998) 2130–2136.
[30] C. Bohn, H. Unbehauen, **Identifikation dynamischer Systeme: Methoden zur experimentellen Modellbildung aus Messdaten**, Springer Vieweg, Wiesbaden, 2016.
[31] R Core Team R, A language and environment for statistical computing, R Foundation for Statistical Computing, Vienna, Austria, 2020.
[32] L.M. Sun, V. Bourdin, Measurement of intracrystalline diffusion by the frequency response method: analysis and interpretation of bimodal response curves, Chem. Eng. Sci. 22 (1993) 3783–3793.
[33] R.G. Jordi, D.D. Do, Analysis of the frequency response method for sorption kinetics in bidispersed structured sorbents, Chem. Eng. Sci. 6 (1993) 1103–1130.
[34] O. Roustant, D. Ginsbourger, Y. Deville, DiceKriging, DiceOptim: Two R packages for the analysis of computer experiments by kriging-based metamodeling and optimization, J. Stat. Softw. 51 (2012) 1–55.
[35] JCGM, Guide to the expression of uncertainty in measurement - GUM 1995 with minor corrections.

[36] N.M. Ridler, M.J. Salter, An approach to the treatment of uncertainty in complex S-parameter measurements, Metrologia 39 (2002) 295.
[37] Y. Wang, M.D. LeVan, Master curves for mass transfer in bidisperse adsorbents for pressure-swing and volume-swing frequency response methods, AIChE J. 57 (2011) 2054–2069.
[38] T. Splith, D. Fröhlich, S.K. Henninger, F. Stallmach, Development and application of an exchange model for anisotropic water diffusion in the microporous MOF aluminum fumarate, J. Magn. Reson. 291 (2018) 40–46.
[39] E. Glueckauf, Theory of chromatography. Part 10.—Formulæ for diffusion into spheres and their application to chromatography, Trans. Faraday Soc. 51 (1955) 1540–1551.
[40] L. Yong, K. Sumathy, Review of mathematical investigation on the closed adsorption heat pump and cooling systems, Renew. Sustain. Energy Rev. 6 (2002) 305–338.
[41] L.M. Sun, F. Meunier, A detailed model for nonisothermal sorption in porous adsorbents, Chem. Eng. Sci. 42 (1987) 1585–1593.
[42] S. Marsili-Libelli, **Environmental Systems Analysis with MATLAB®**, CRC Press, Boca Raton, 2016.
[43] W. Kast, **Adsorption aus der Gasphase: Ingenieurwissenschaftliche Grundlagen und technische Verfahren**, VCH, Weinheim, 1988.
[44] D. Bathen, M. Breitbach, Adsorptionstechnik, VDI-Buch, Springer, Berlin, Heidelberg, 2001.
[45] J.M. Gurgel, L.A. Filho, P. Grenier, F. Meunier, Thermal diffusivity and adsorption kinetics of silica-gel/water, Adsorption 7 (2001) 211–219.
[46] M.G. Kaganer, Thermal Insulation in Cryogenic Engineering, Israel Program for Scientific Transl., Jerusalem, Jerusalem, 1969.
[47] J. Kärger, C. Chmelik, L. Heinke, R. Valiullin, A new view of diffusion in nanoporous materials, Chem. Ing. Tech. 82 (2010) 779–804.
[48] E. Laurenz, A. Velte, H. Kummer, G. Füldner, L. Schnabel, Adsorption dynamics of MOF coatings for waste heat driven cooling, in: Proceedings of the 25th IIR International Congress of Refrigeration, International Institute of Refrigeration (IIR), France, 2019.
[49] A. Frazzica, G. Füldner, A. Sapienza, A. Freni, L. Schnabel, Experimental and theoretical analysis of the kinetic performance of an adsorbent coating composition for use in adsorption chillers and heat pumps, Appl. Therm. Eng. 73 (2014) 1022–1031.